Earth and Planetary Science Letters 460 (2017) 244–254

Contents lists available at ScienceDirect

Earth and Planetary Science Letters

www.elsevier.com/locate/epsl

Lithospheric density structure beneath the Tarim basin and surroundings, northwestern China, from the joint inversion of gravity and topography

Yangfan Deng [a,b,*], Will Levandowski [c], Tim Kusky [d]

[a] State Key Laboratory of Isotope Geochemistry, Guangzhou Institute of Geochemistry, Chinese Academy of Sciences, Guangzhou 510640, China
[b] Department of Geology, University of Illinois at Urbana–Champaign, Champaign, IL 61820, USA
[c] U.S. Geological Survey, Geological Hazards Science Center, Denver, CO 80225, USA
[d] State Key Lab for Geological Processes and Mineral Resources, Center for Global Tectonics, School of Earth Sciences, China University of Geosciences, Wuhan, 430074, China

ARTICLE INFO

Article history:
Received 18 April 2016
Received in revised form 22 October 2016
Accepted 25 October 2016
Available online 14 December 2016
Editor: A. Yin

Keywords:
joint inversion
lithospheric density
Tarim basin
oceanic plateau
strain partition
depleted mantle lithosphere

ABSTRACT

Intraplate strain generally focuses in discrete zones, but despite the profound impact of this partitioning on global tectonics, geodynamics, and seismic hazard, the processes by which deformation becomes localized are not well understood. Such heterogeneous intraplate strain is exemplified in central Asia, where the Indo-Eurasian collision has caused widespread deformation while the Tarim block has experienced minimal Cenozoic shortening. The apparent stability of Tarim may arise either because strain is dominantly accommodated by pre-existing faults in the continental suture zones that bound it—essentially discretizing Eurasia into microplates—or because the lithospheric-scale strength (i.e., viscosity) of the Tarim block is greater than its surroundings. Here, we jointly analyze seismic velocity, gravity, topography, and temperature to develop a 3-D density model of the crust and upper mantle in this region. The Tarim crust is characterized by high density, v_s, v_p, and v_p/v_s, consistent with a dominantly mafic composition and with the presence of an oceanic plateau beneath Tarim. Low-density but high-velocity mantle lithosphere beneath southern (southwestern) Tarim underlies a suite of Permian plume-related mafic intrusions and A-type granites sourced in previously depleted mantle lithosphere; we posit that this region was further depleted, dehydrated, and strengthened by Permian plume magmatism. The actively deforming western and southern margins of Tarim—the Tien Shan, Kunlun Shan, and Altyn Tagh fault—are underlain by buoyant upper mantle with low velocity; we hypothesize that this material has been hydrated by mantle-derived fluids that have preferentially migrated along Paleozoic continental sutures. Such hydrous material should be weak, and herein strain focuses there because of lithospheric-scale variations in rheology rather than the pre-existence of faults in the brittle crust. Thus this world-class example of strain partitioning arises not simply from the pre-existence of brittle faults but from the thermo-chemical and therefore rheological variations inherited from prior tectonism.

1. Introduction

How and why intraplate strain becomes focused in discrete zones is a first-order problem in geodynamics, and the mélange of lithospheric fragments that constitute central Asia provide one of the best examples in the world of such strain partitioning. Individual terranes separated by Paleozoic continental suture zones exhibit disparate rates and styles of deformation, with the Tarim block in particular apparently remaining stable and essentially undeformed amidst widespread tectonism.

Having previously been attached to the Rodinian supercontinent, Tarim was an isolated block of multiply deformed Archean lithosphere until Paleozoic collisions with the Qaidam terrane on its southern margin and then the Yili block on its northern margin (Zhang et al., 2013). Boreholes and seismic reflection profiles reveal that these accretionary events created up to ~5 km of throw on fault-cored anticlines in north-central Tarim (Liu et al., 2016). Shortly thereafter (early Permian), a mantle plume impinged upon the base of the lithosphere beneath Tarim, melting already refractory mantle lithosphere and emplacing mafic–

* Corresponding author at: State Key Laboratory of Isotope Geochemistry, Guangzhou Institute of Geochemistry, Chinese Academy of Sciences, Guangzhou 510640, China.
E-mail addresses: yangfandeng@gig.ac.cn (Y. Deng), wlevandowski@usgs.gov (W. Levandowski).

http://dx.doi.org/10.1016/j.epsl.2016.10.051
0012-821X/

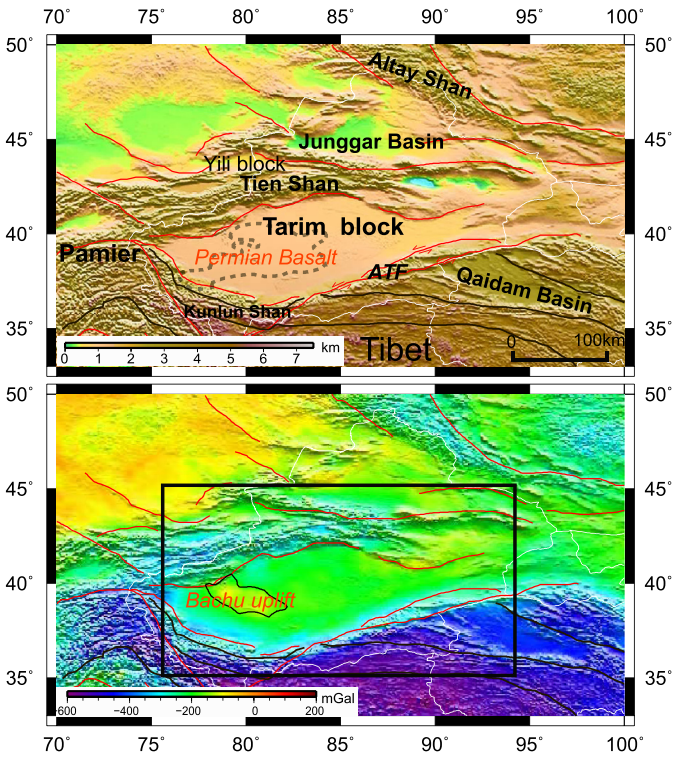

Fig. 1. (a) Topography (Etopo1, www.ngdc.noaa.goc/mgg/global/global.html) and (b) Bouguer gravity (EGM2008, Pavlis et al., 2012) in the Tarim block and surrounding regions. The red lines indicate the faults; the solid brown lines in Tibet indicate the tectonic boundaries. The dotted brown contour indicates the region of Permian basalt; the black solid contour indicates the region of Bachu. The black box indicates our study region. ATF: Altyn Tagh Fault. (For interpretation of the references to color in this figure legend, the reader is referred to the web version of this article.)

ultramafic intrusions and A-type granites over 250,000 km^2 in the southern and western parts of the block (Zhang et al., 2013; Xu et al., 2014) (Fig. 1).

The Cenozoic collision of India with Eurasia has reactivated deformation in the Kunlun Shan to the southwest of the Tarim block, the Tibetan Plateau to the south, the Altyn Tagh fault to the southeast, and the Tien Shan to the north. Yet Tarim is characterized by low heat flow (Feng et al., 2009), few earthquakes (Teng et al., 2014), and little Cenozoic deformation (e.g., Guo et al., 2005) in its interior. As such, deformation in central Asia resembles a kinematic block model in which slip is mostly confined to the fault zones that separate a number of discrete, stable microplates (e.g., Tapponnier and Molnar, 1976). Hypothesized causes of this partitioned strain can be broadly categorized as those that suggest that the pre-existence and frictional properties of faults decouple distinct terranes (e.g., Tapponnier et al., 2001) or those that invoke anomalous strength of the Tarim lithosphere as a whole (e.g., Neil and Houseman, 1997; Calignano et al., 2015). Insofar as weakness is most often ascribed to faults in the brittle crust but strength is ascribed to a high-viscosity mantle, these two classes of hypotheses implicitly make predictions and/or assumptions about the relative importance of the brittle and ductile regimes to intraplate seismicity. Nevertheless, up to 15 km of Paleozoic–Cenozoic sediments (e.g., Guo et al., 2005) obscure the geologic and geodynamic underpinnings of Tarim's apparent stability, complicating efforts to distinguish between the two classes of hypotheses.

The first class of models offers a relatively simple explanation for the lack of deformation in the Tarim block: Strain focuses on pre-existing faults in the continental suture zones that bound this once-isolated terrane, and little stress is transmitted across them into the interior of Tarim block. Indeed, Neogene-ongoing reactivation of the Tien Shan (Hendrix et al., 1994) exploits the faults inherited from Paleozoic accretion, with Tarim again underthrusting beneath the range (e.g., Windley et al., 1990). Similarly, the modern Altyn Tagh fault occupies the boundary between Tarim and the Qaidam block (Yin et al., 2002) and remains a profound lithospheric-scale feature, focusing sinistral shear in a zone less than 40 km wide (Wittlinger et al., 1998). Despite explaining the Cenozoic stability of Tarim, such models generally require slip rates higher than those observed geodetically (e.g., Bendick et al., 2000) or geomorphologically (e.g., Cowgill et al., 2009). They also do not explain why the reverse faults active in the Paleozoic in central Tarim are now quiescent (e.g., Guo et al., 2005; Liu et al., 2016), and do not easily unify crustal deformation, topographic growth, and geodynamic evolution (e.g., England and McKenzie, 1982).

If instead the Tarim block remains stable because it is stronger than its surroundings, a mechanism for this strength must be identified. Proposed causes of such cratonization generally call upon an oceanic affinity of the Tarim lithosphere, either a remnant oceanic basin (Hsü, 1988) or a trapped Precambrian oceanic plateau (Kusky and Mooney, 2015) similar in geophysical character to that beneath the Caspian Sea (e.g., Sengor, 1979). Indeed there is seismic evidence for lithosphere thicker than 160 km beneath Tarim (e.g., Bao et al., 2015), which is more characteristic of oceanic plateaus—with crustal thicknesses of 30–40 km and sub-crustal lithospheric thicknesses exceeding 100 km—than of trapped ocean basins, which would have significantly thinner crustal and mantle lithosphere (e.g., Kusky and Mooney, 2015). Nevertheless, a deep drill-core sample of Neoproterozoic diorite beneath central Tarim is unusual for oceanic crust (Guo et al., 2005), although dioritic to tonalitic rocks are known from several oceanic plateaus (Kusky and Mooney, 2015). Additionally, widespread Paleozoic unconformities within the Tarim block (Liu et al., 2016) suggest that the Cenozoic stability of the Tarim block cannot be ascribed to lithospheric strength inherited from prior to the latest Paleozoic.

Alternatively, processes since the late Paleozoic may have led to cratonization in at least some parts of the Tarim block. Specifically, the high-temperature extraction of melts from the mantle lithosphere that is documented in the voluminous plume-related Permian intrusions (Zhang et al., 2013; Xu et al., 2014) in southern and western Tarim (Fig. 1) may have removed hydrous, aluminous, and iron-rich phases, leaving behind a residue with increased modal Mg and olivine but decreased garnet and clinopyroxene and therefore decreased density (e.g., Schutt and Lesher, 2010) and increased viscosity (e.g., Lee et al., 2001).

These three possibilities—that Tarim is not underlain by material with anomalous strength and therefore stability results from decoupling of discrete terranes by faults in the continental sutures zones that bound it; that Tarim overlies ancient, thick, mafic–intermediate lithosphere; and that the lower mantle has been depleted and dehydrated by plume magmatism specifically beneath the known extent of Permian intrusions—imply different predictions about the velocity and density structure of the crust and upper mantle beneath the basin relative to its surroundings. Broadly homogeneous mantle lithosphere is most consistent with dominant control by pre-existing faults in the brittle regime. A thick, ancient thermal root would have high velocity and high density. Finally, cold and depleted mantle lithosphere should have high velocity in accordance with its temperature but comparatively lower density because of its compositional buoyancy.

To this end, we combine the S-velocity model of Bao et al. (2015), the crustal thermal model of Sun et al. (2013), gravity, and topography to develop a 3D density model of the crust and upper mantle (to 200 km depth) beneath the Tarim block and its surroundings. In turn, we discuss the rheologic variations suggested by this structure and explore their implications for the origin of the Tarim block and for regional seismotectonics.

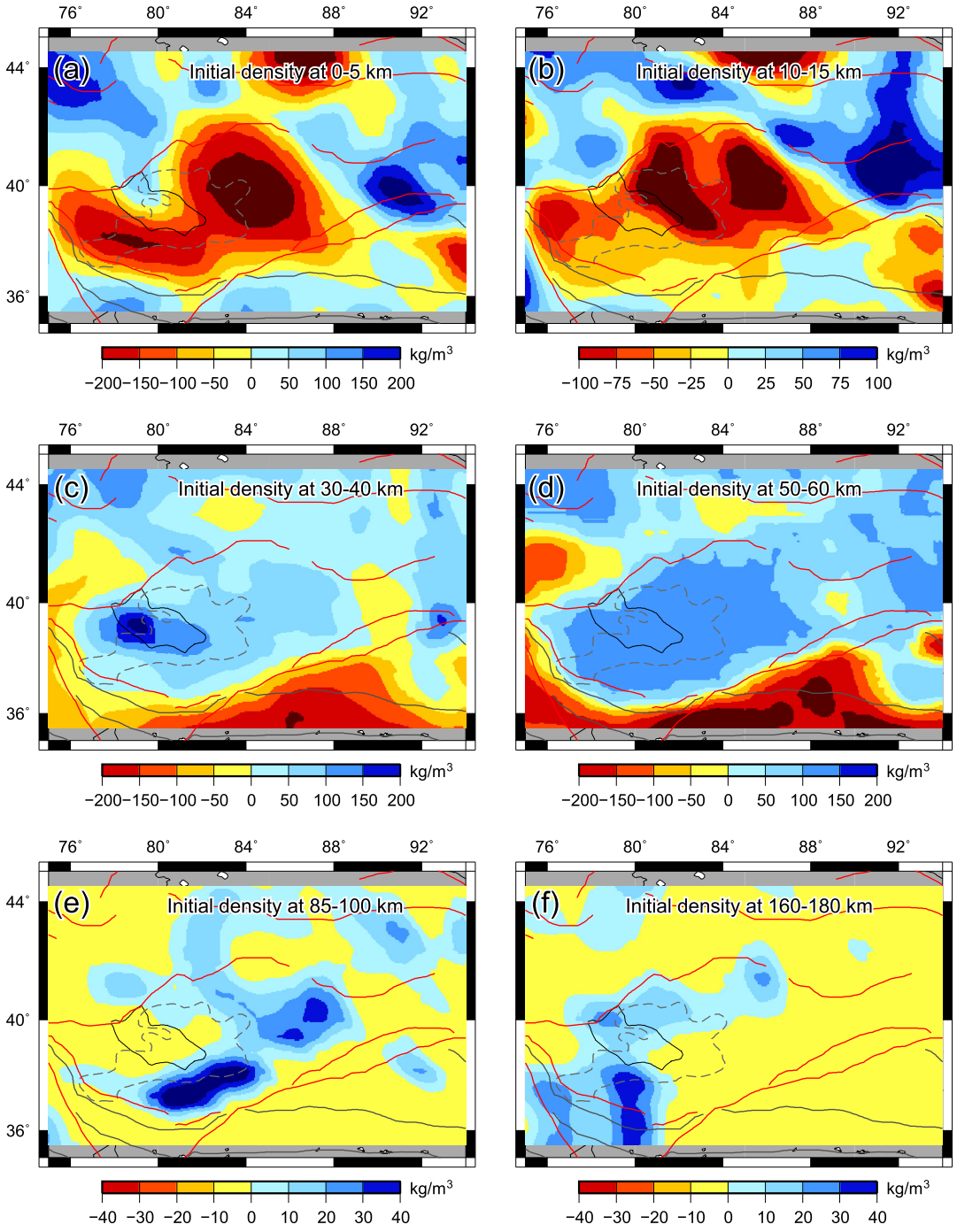

Fig. 2. Initial density variations estimated from seismic velocity and temperature (the mean is removed from each layer for ease of comparison) at 0–5 km, 10–15 km, 30–40 km, 50–60 km, 85–100 km, 160–180 km depth. (For interpretation of the colors in this figure, the reader is referred to the web version of this article.)

2. Density modeling

Gravity anomalies are often used to investigate lithospheric density, but solutions derived from gravity alone are inherently non-unique. Complementary constraints on the density structure such as flexurally modulated topography and supplemental constraints such as seismic velocity, however, allow for the generation of more robust density models (e.g., Sheehan and Solomon, 1991). We derive a 3D starting model of crustal and upper mantle density (Fig. 2) from the seismic velocity of Bao et al. (2015), who combined ambient noise and earthquake data by measuring more than 700,000 dispersion curves to generate group and phase velocity maps at periods of 10–140 s. Nevertheless, because of the remoteness and scarcity of seismic stations within the Tarim basin, Bao et al. report lateral resolution of only ~200 km in parts of our study area. Both in order to improve this resolution (e.g., Maceira and Ammon, 2009) and to explore the longer-wavelength relationship between velocity and density, which has implications for lithospheric rheology, we then employ the random-walk algorithm of Levandowski et al. (2015) to iteratively refine this density model until it simultaneously reproduces gravity and topography to within 10 mGal and 100 m. In contrast to previous studies that generate only one density model (e.g., from gravity; Deng et al., 2014), this method is capable of finding thousands of plausible solutions, embracing the non-uniqueness of the problem while simultaneously satisfying multiple complementary observables.

2.1. The initial density model and sources of systematic error

2.1.1. Crustal density

An initial estimate of crustal density (Fig. 2) is derived from the seismic velocities reported by Bao et al. (2015) using the velocity-density scaling (Brocher, 2005):

$$\rho = 1.6612 \cdot v_p - 0.4721 \cdot v_p^2 + 0.0671 \cdot v_p^3 - 0.0043 \cdot v_p^4 + 0.000106 \cdot v_p^5 \quad (1)$$

We initially assume a constant v_p/v_s ratio of 1.78. This relationship is well suited to intermediate compositions but broadly has the bias to overestimate the density of felsic rocks and underestimate the density of mafic material (e.g., Levandowski et al., 2014).

Nevertheless, velocity and density are both sensitive to temperature as well as to composition. Considering crustal material with a density of 2847 kg/m^3, v_s of 3.6 km/s, v_p/v_s of 1.78, coefficient of thermal expansion of 2.5×10^{-5}/°C, and $\partial v_p/\partial T$ of 0.5 m/s per °C (Christensen and Mooney, 1995), a 100 °C temperature increase would decrease density by 7 kg/m^3 and velocity by 0.03 km/s. By contrast, a similar velocity decrease due to composition is modeled as a 13 kg/m^3 density decrease (eq. (1)). That is, increasing temperature leads to a density underestimate of 6 kg/m^3 per 100 °C (0.06 kg/m^3 per 1 °C). Therefore, hot material is *denser* than predicted by eq. (1), and cold material is less dense than predicted.

Consequently, after scaling crustal velocity to density using eq. (1), the estimated density is corrected for departures from an arbitrary reference crustal geotherm—15 °C/km (Levandowski et al., 2015)—using the temperature model (T) of the crust from Sun et al. (2013), who joined the 3D steady-state heat transfer equations with borehole heat flow data.

Hence the temperature anomaly relative to our arbitrary reference geotherm is:

$$\Delta T(x, y, z) = T(x, y, z) - T_{ref}(z) = T(x, y, z) - 22.6 \cdot (z + Elevation(x, y)), \quad (2)$$

where z is the depth below sea level. The attendant density correction is

$$\rho(x, y, z) = \rho_0(x, y, z) + 0.06 \cdot \Delta T(x, y, z) \quad (3)$$

Melt also strongly affects velocity. The presence of 1% partial melt only decreases bulk density by 0.12% (Humphreys and Dueker, 1994) but v_s by 7.9% (Hammond and Humphreys, 2000). From eq. (1), the presence of 1% partial melt would cause us to underestimate density by some 120 kg/m^3.

2.1.2. Mantle density

Mantle densities and velocities also vary laterally as functions of temperature and composition, but it is difficult to disentangle their relative contributions from tomographic images alone (Mooney and Kaban, 2010). Therefore, we will first assume that the mantle is isochemical and that all lateral velocity variations reflect temperature variations (this assumption will subsequently be relaxed). We use published estimates of bulk and shear moduli and their pressure- and temperature-derivatives along with temperature-dependent thermal expansivities for olivine, garnet, spinel, orthopyroxene, and clinopyroxene to estimate elastic S-velocity as a function of temperature. Then, we account for anelastic reductions of velocity by calculating the Laplace transform of the temperature-, pressure-, and seismic-period-dependent creep function (See more details in Levandowski et al., 2015).

Across a wide range of mineralogies ($r^2 > 0.9$), the density variations relative to a reference (assumed to be the solidus) at which density $= \rho_0$ and velocity $= v_0$ are given by

$$\Delta\rho = \Delta v_s \times \left(7.3 - \frac{z}{100\text{ km}} + \frac{\Delta v_s}{4}\right); \quad \Delta v_s \le 6\% \quad (4a)$$

$$\Delta\rho = \Delta v_s \times \left(8.8 - \frac{z}{100\text{ km}} - \frac{7(\Delta v_s - 6)}{40}\right); \quad \Delta v_s \ge 6\% \quad (4b)$$

Here, Δv_s is the anomaly (in %) relative to v_0, which we assume to be 4.5 km/s (Sato et al., 1989 and therein).

$$\Delta v_s = 100 * (v_s - v_0)/v_0 \quad (4c)$$

Since the reference is meant to be the solidus (i.e., assuming that the adiabatic temperature in the asthenosphere is quite near the solidus), velocities below v_0 may reflect increasing melt content, which does not affect density. Therefore, there is a final implicit segment of the piecewise-continuous velocity-density relationship:

$$\Delta\rho = 0; \qquad \Delta v_s \le 0\% \quad (4d)$$

This velocity-density scaling ignores compositional variations, the most important of which is likely to be differences between fertile and depleted upper mantle (e.g., Godey et al., 2004). Specifically, extraction of melt preferentially removes iron, volatiles, and aluminous phases such as garnet and spinel, leaving behind a dry residue enriched in olivine and magnesium. Empirical correlations among Mg# (Mg# == [Mg]/[Mg + Fe]), seismic velocity, and density suggest that a unit increase in Mg# correlates with a ~0.4% (~13 kg/m^3) decrease in density and a ~0.25% (~0.01 km/s) increase in velocity (Schutt and Lesher, 2010). Since the latter would be modeled as a 2 kg/m^3 increase in density, a unit increase in Mg# leads to a density overestimate of 15 kg/m^3 using eqs. (4).

Similarly, the introduction of water into peridotite lowers velocity but drastically lowers density (Christensen, 2004). A density decrease of 0.5% (~16 kg/m^3) accompanies each 1% decrease in velocity. The decrease in density associated with 1% hydration-induced slowing is twice as great as the density decrease associated with 1% heating-induced slowing (Christensen, 2004; Levandowski et al., 2015). Therefore, scaling seismic velocity to density under the assumption that mantle wavespeed-variations solely reflect lateral temperature heterogeneity should lead to underpredicted elevations in areas of hydrous mantle lithosphere. Although the seismic model of Bao et al. (2015) has a lateral resolution of only 200 km in some parts of our study area, we note that mantle temperature variations are generally of similar or greater lengthscales. Thus, both seismic velocity itself and the input seismic velocity model should be sensitive to mantle temperature, but either or both may be blind to mantle compositional variations.

2.2. Refining the density model

The initial density model predicts local isostatic topography, E (Lachenbruch and Morgan, 1990):

$$E = H - H_0; \quad H = \int_0^{z_a} \frac{\rho_a - \rho(z)}{\rho_a} dz. \quad (5)$$

H_0 is a correction term of 2.4 km to achieve isostatic equilibrium with an asthenospheric column (water-stripped mid-ocean ridges).

Lithospheric flexural strength modulates local buoyancy. Convolution of E with the flexural filter of the lithosphere, F, accounts for such flexural smoothing and yields the smoothed surface elevation field $\varepsilon_{predicted}$ that is predicted by the 3D density model:

$$\varepsilon_{predicted} = E \cdot F. \quad (6)$$

F is a system of zero-order Kelvin–Bessel functions (Watts, 2001, equations (3.54)–(3.55)). We estimate the elastic thickness

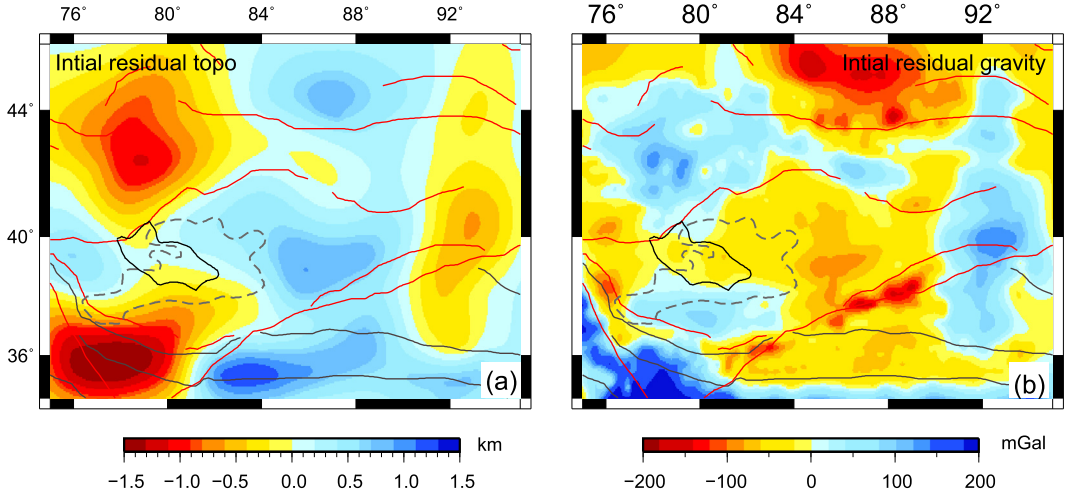

Fig. 3. Residual topography and gravity attendant to the initial, seismically derived model. Negative residual topography (warm colors) denotes regions in which the densities estimated from seismic velocity and temperature are too high: the Kunlun Shan and western Tien Shan. Negative residual gravity denotes regions in which the initial densities are too low. Note, for example, the ~100 km-wide anomaly coincident with the Altyn Tagh Fault. Features of this scale are below the resolution of the seismic velocity model and therefore may reflect sharp boundaries in crustal structure that are smeared horizontally in the starting model rather than locally anomalous lithologies (compare the smooth crustal structure in Fig. 2 and the sharp gravity gradient shown in Fig. 1b). (For interpretation of the colors in this figure, the reader is referred to the web version of this article.)

in two-dimensions across the region by the multitaper spectral estimation method (Pérez-Gussinyé et al., 2004).

Similarly, the convolution of observed surface elevations with F produces a smoothed elevation field, $\varepsilon_{observed}$. For the estimated lithospheric density structure to be plausible, $\varepsilon_{predicted}$ must match $\varepsilon_{observed}$ within some tolerance (again, we choose 0.1 km).

Our gravity calculations are quite similar to the approach of Maceira and Ammon (2009), with two exceptions. First, our grid is laterally uniform–comprising 31×31 km horizontal grids (vertical dimensions of 5–10 km in the crust and 10–20 km in the mantle)–rather than $1^\circ \times 1^\circ$. Second, our gravity kernel at a given surface node considers the effects of all cells in the model (as opposed to only considering cells within a certain radius). Following Bao et al., we assign the 4.0 km/s iso-velocity contour as the Moho. Because our parameterization features 10 km-thick layers in the lower crust and upper mantle, however, we find in sensitivity tests (not shown) that minor changes in this value do not strongly affect our results apart from moving the predicted elevation all across the study area up or down.

The gravity and topography predicted by the initial density model are imperfect matches to observations. The residual topography (H_r) and gravity (G_r) highlight these discrepancies (Fig. 3):

$$G_r = G_{predicted} - G_{observed}; \qquad H_r = \varepsilon_{predicted} - \varepsilon_{observed} \tag{7}$$

Refining the density model to reconcile these residuals can produce acceptable estimates of the density of Tarim and its surroundings. To do so, we employ the random-walk Monte Carlo algorithm of Levandowski et al. (2015), which iteratively refines the 3D starting model until gravity and flexurally modulated topography are simultaneously reproduced to within 10 mGal and 100 m at all points in the study area. At short wavelengths, these adjustments may simply represent features below the resolution of the surface wave model (e.g., Maceira and Ammon, 2009). More spatially extensive adjustments (Fig. 4) plausibly reflect compositional variations in the mantle lithosphere and anomalous v_p/v_s ratios in the crust (e.g., the density of mafic material is systematically underestimated by such a starting model).

Because gravity and topography are inherently non-unique functions of the 3-D density structure, we conduct 1000 Monte Carlo simulations–beginning from the density model derived from the velocities of Bao et al. and equations (1)–(4) and stochastically adjusting it until gravity and topography are reproduced to within 10 mGal and 100 m at all points in the study area, ultimately creating a 1000-member posterior distribution of plausible 3-D density structures. We discuss the mean across those 1000 plausible densities at any given point (Fig. 5). Because of the large number of models, the uncertainty of that mean value is universally small (Levandowski et al., 2015). One synthetic test is shown in the supplement to assess the method used in this region.

3. Results

3.1. Tarim

The Tarim basin hosts sediments and metasedimentary rocks to depths of 5–15 km (Guo et al., 2005; Liu et al., 2016), and both v_s and density at 0–5 km reflect this material (Figs. 2a, 5a). Yet beneath the Bachu Uplift, where the sedimentary cover is thinnest (Yang and Liu, 2002), we image denser material than anywhere else in the basin (Fig. 5b). This material is not captured in the seismic velocity model (Fig. 2b), likely because of its small lateral dimension, so its appearance in the density highlights the effectiveness of considering gravity and topography in imaging crustal structure. This result is similar to the finding of Maceira and Ammon (2009) that joint inversion of gravity and surface wave dispersion for shear-velocities improves resolution of shallow *velocity* structure.

Dense lower crust appears from 20–40 km beneath Tarim, and the highest densities coincide closely with the extent of Permian magmatism (Figs. 2c, 5c). This material is slightly denser than estimated from seismic velocity alone, also consistent with the elevated v_p/v_s expected with an abundance of mafic material (e.g., Levandowski et al., 2015).

High-density mantle bounds Tarim to the north from 60 to 200 km depth (Figs. 2e–f, 5e–f). This body manifests in both seismic velocity and density, and it dips steeply northward (Fig. 6), consistent with previous seismological evidence that the Tarim lithosphere was partially subducted beneath the Tien Shan in the Paleozoic (Windley et al., 1990) and/or is currently underthrusting the range (e.g., Vinnik et al., 2006; Lei and Zhao, 2007; Li et al., 2009).

By stark contrast, the mantle lithosphere beneath southern (southwestern) Tarim is less dense than the relatively high velocity suggests (Figs. 4e–f) and achieves buoyancy similar to the

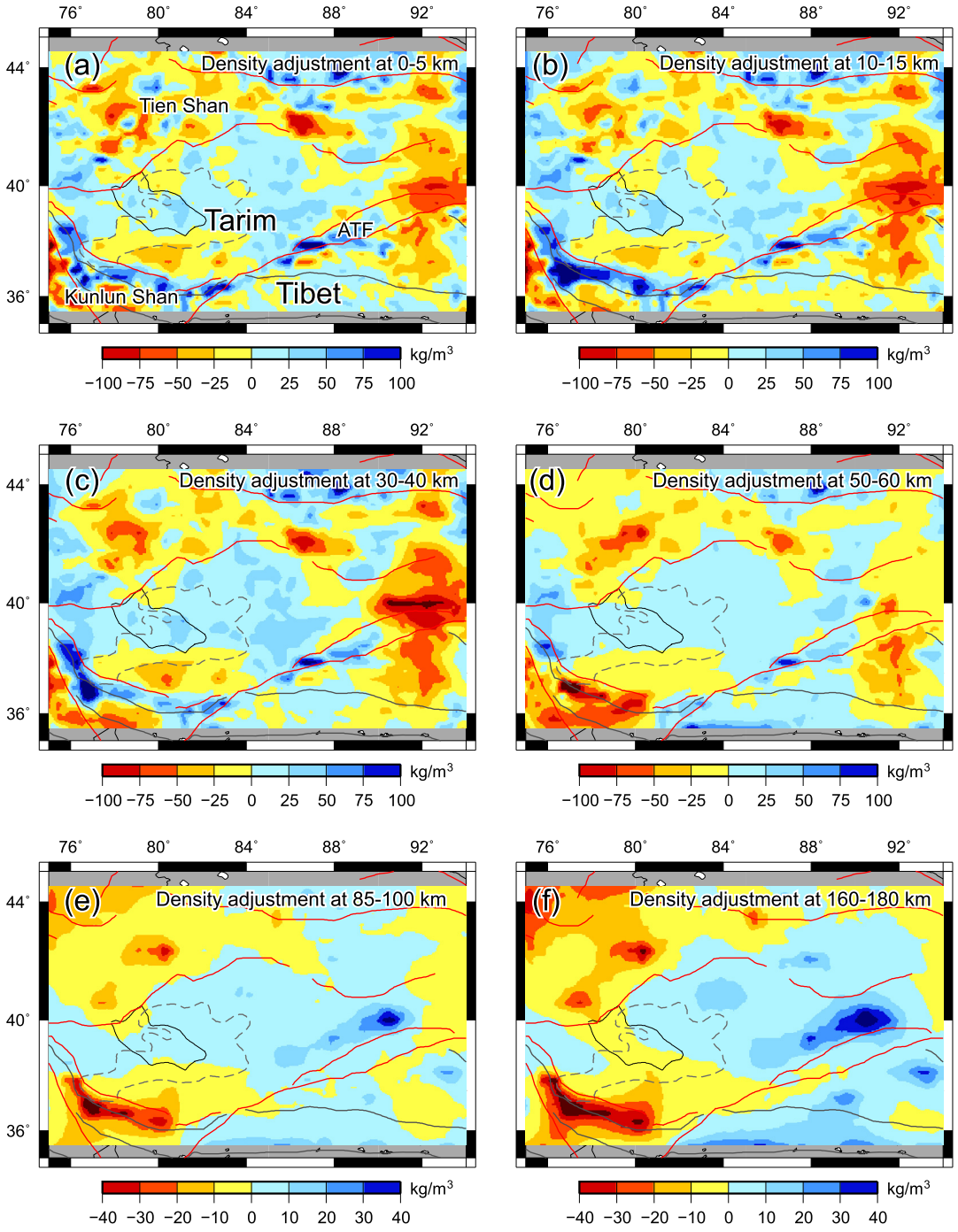

Fig. 4. Density adjustments required to reproduce gravity and topography, relative to the density model shown in Fig. 2. (For interpretation of the colors in this figure, the reader is referred to the web version of this article.)

upper mantle beneath the tectonically active Kunlun Shan and Tien Shan (Figs. 5e–f, 6). This anomaly appears as a linear, NW-SE band that partly underlies the extent of Permian magmatism (Figs. 4e–f, 5e–f, 6), supporting the hypothesis that the mantle lithosphere was melt-depleted by a mantle plume.

3.2. The Tien Shan

The Tien Shan is variably underthrust by the northern margin of the Tarim block, and the overriding mantle has low velocity (Figs. 2e–f). Yet especially at the boundary between Tarim and the Yili block (western Tien Shan), this upper mantle material is less dense than predicted by eq. (4) (Figs. 4e–f, 6). Although lithospheric thinning (and replacement by asthenosphere) would cause a higher temperature and thus lower velocity, this couldn't explain the negative density adjustment (e.g., Lee et al., 2001; Schutt and Lesher, 2010). We therefore suggest that this buoyant material is intact mantle lithosphere with a source of chemical (i.e., non-thermal) buoyancy.

One possibility is that the plume responsible for Permian volcanism spread along the base of the thick Tarim lithosphere until it reached the margins of the craton, where it caused the mantle lithosphere melted further, incorporating fractions of the adjacent lithosphere. As such, this buoyant material on the flanks of the Tarim block may be melt-depleted mantle lithosphere. However, melt-depleted and therefore higher-viscosity mantle beneath the

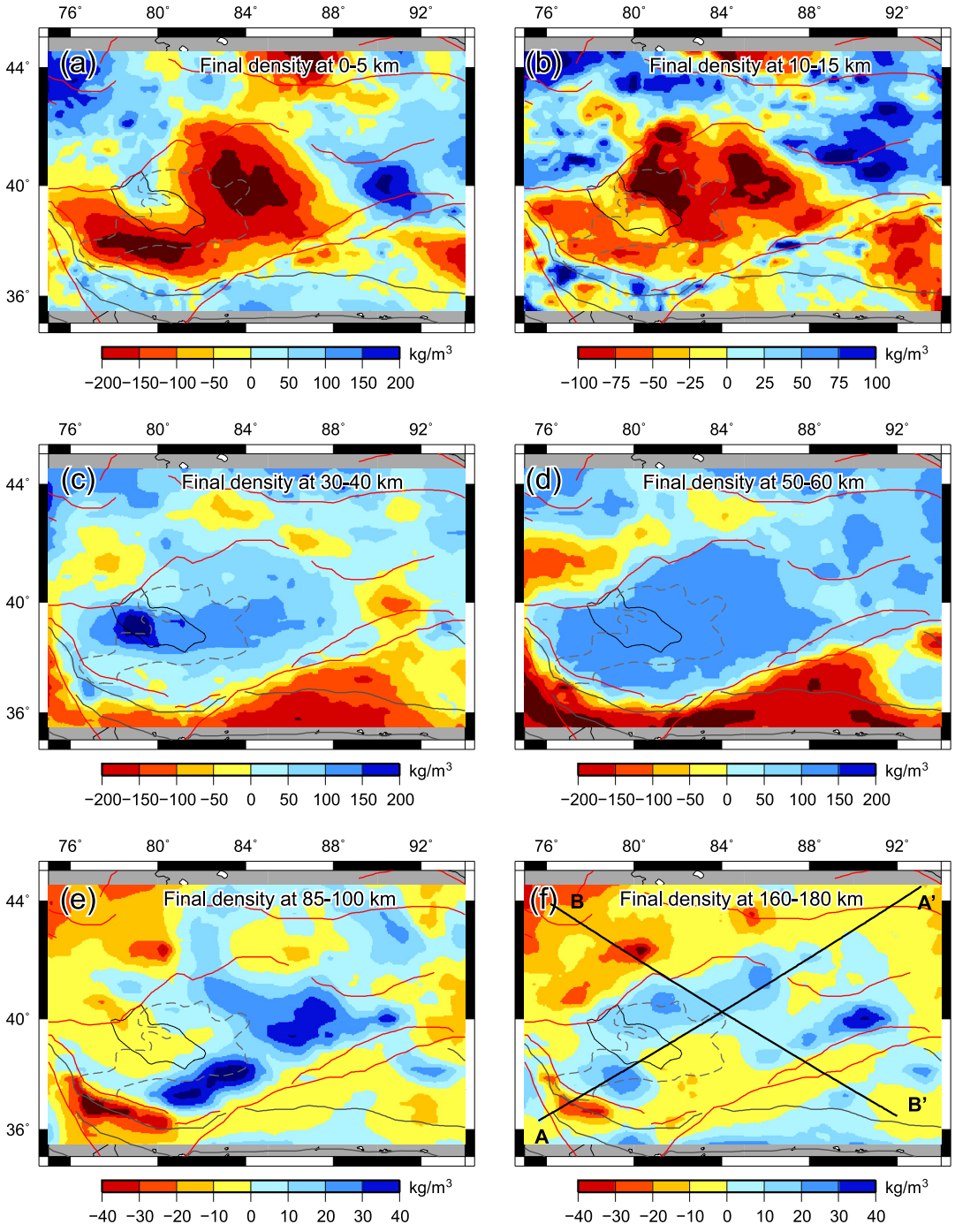

Fig. 5. Final density model averaged over the 1000 simulations. The mean has been removed from each layer. Cross sections (A–A′, B–B′) are shown in Fig. 6f. (For interpretation of the colors in this figure, the reader is referred to the web version of this article.)

Tien Shan would be more resistant to deformation than its surroundings, so the observed focusing of strain in these zones would be even more puzzling. Furthermore, the occurrence of Permian basalts over a region extending more than 1000 km across the Tarim basin (rather than sequestered along its edges) is at odds with this hypothesized edge-driven convection.

Alternatively, an influx of fluid from the subducting Tarim lithosphere could generate paragasite/antigorite in the uppermost mantle, and amphibole and phlogopite at greater depths. Such hydration-induced retrogression decreases velocity but drastically decreases density: approximately 16 kg/m^3 for each corresponding 1% velocity reduction (e.g., Christensen, 2004; Hacker and Abers, 2004), roughly twice the slope given by eq. (4) (∼7 kg/m^3 per 1% v_s perturbation). Since we find that the density of this material is indeed less than we initially estimated with eq. (4), the anomalous upper mantle beneath the Tarim–Tien Shan boundary most plausibly reflects preferential migration of fluids along the lithospheric-scale fracture network where the Yili block abuts Tarim above the subducting material.

The crust of the Tien Shan is thicker than its surroundings (e.g., Bao et al., 2015), and this buoyancy is manifest in low densities from 50–60 km (Fig. 5d). Additionally, a negative velocity gradient in the upper crust (v_s at 15 km is greater than at 30 km) resembles the signature of melt in the mid-crust, but the fact that the

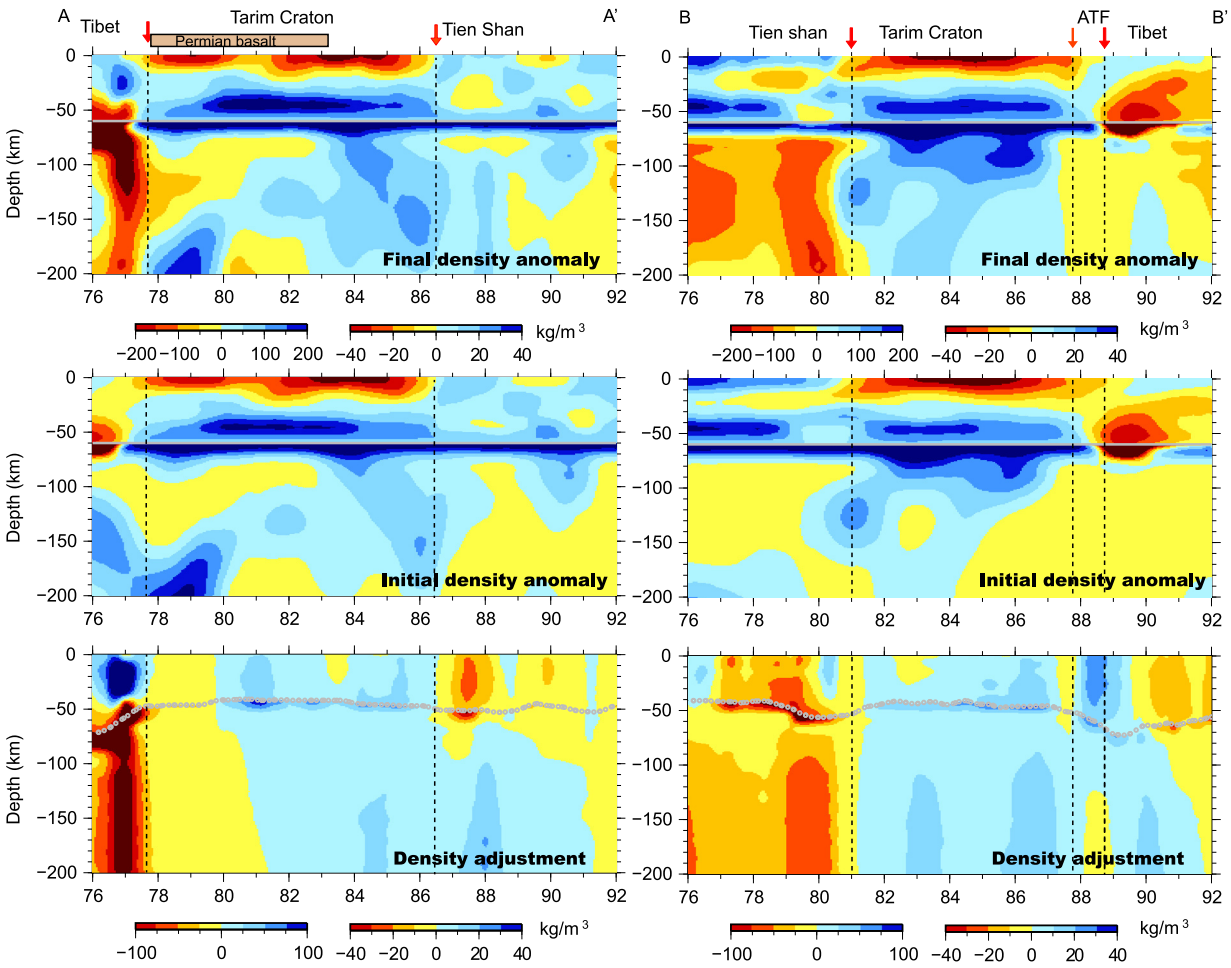

Fig. 6. Cross sections through the mean final density model. Locations are shown on Fig. 5. The lines at 60 km are used to divide the density anomaly into two parts with different color-scales ($-100 \sim +100$ kg/m^3 for the upper part, $-40 \sim +40$ kg/m^3 for the lower part). The dotted gray lines in the lower panels indicate Moho depth. (For interpretation of the colors in this figure, the reader is referred to the web version of this article.)

modeled density in this depth range is less than the starting value (Fig. 2c) indicates low v_p/v_s, which is inconsistent with the presence of partial melt.

Instead, two possible explanations for this feature are negative anisotropy and felsic rocks in the middle-lower crust. Xie et al. (2013) report ~3% negative radial anisotropy ($v_{sv} > v_{sh}$) in the mid-crust of the Longmenshan region; if steeply dipping foliation is similarly present in the mid to lower crust beneath the Tien Shan, it would lead to an overestimate of the isotropic v_s and thus of density. Alternatively, an imbricate wedge of felsic material could explain the negative velocity gradient, low density, and low v_p/v_s inferred in the middle-lower crust of the Tien Shan. We cannot distinguish between these two possibilities with the data and models at hand.

3.3. The Pamir and Kunlun Shan

Similar to the Tien Shan, the Pamir and Kunlun Shan overlie buoyant upper mantle (Figs. 5e–f), and again this feature coincides with the juxtaposition of two distinct lithospheric blocks. Notably, the mantle beneath the Kunlun Shan is more buoyant than beneath topographically higher Tibet, farther south. Indeed, despite heterogeneous velocities, a nearly continuous band of buoyant upper mantle rings the western and southern margins of Tarim from the western Tien Shan to the Qaidam basin (i.e., the Altyn Tagh fault). This ring is generally less than 200 km-wide and so may not have been imaged seismically. Nevertheless, it is improbably narrow for a thermal anomaly (the densities imaged would require a +300 °C anomaly), and therefore—as discussed above—we favor the interpretation that fluids from material subducted during continental suturing have preferentially migrated along these suture zones, causing hydration-induced retrograde metamorphism and attendant density loss.

Unlike the upper mantle, the crust beneath the Kunlun Shan is not anomalous compared with the rest of the region to the south (Figs. 5a–d). Although a narrow band of crust along the southern margin of Tarim is denser than the seismic velocity indicates, Bao et al. (2015) report lateral resolution of only 200 km in western China. Consequently, the starting model contains a smooth transition across these boundaries (Fig. 2), but the adjustments to this starting model (Fig. 4) generally serve to remove this gradient such that a sharp boundary is recovered (Fig. 5).

3.4. The Altyn Tagh Fault

Because features with lateral extent less than ~200 km are not well resolved by the seismic velocity model (Bao et al., 2015), the border between Tarim and Tibet is a smooth transition in our initial model (Fig. 2), inconsistent with the known juxtaposition of distinct terranes (e.g., Kao et al., 2001) and the structural heterogeneity seen in more focused seismic studies (e.g., Wittlinger et al., 1998). However, the smooth transition in the seismic velocity model is almost entirely erased by the density refinements,

exemplifying the utility of joint consideration of continental-scale seismic models, gravity, and topography.

In the final density models, the upper mantle beneath the Altyn Tagh Fault is anomalously buoyant (similar to the low velocities reported by Wittlinger et al., 1998), marking the eastern extent of the buoyant material bounding west and south Tarim that we propose to be lithosphere hydrated by mantle-derived fluids that have preferentially migrated along lithospheric-scale fracture zones.

In addition to the steep topographic gradient across the fault (Fig. 1a), it juxtaposes sedimentary fill of the Tarim basin with bedrock of northern Tibet (Figs. 5, 6) and the thickened crust in Tibet from upper mantle beneath Tarim (Figs. 5, 6). Given the low resolution of the starting crustal models, we cannot at present discriminate between the possibilities that the positive density adjustment simply recovers the juxtaposition of discrete terranes or that it reflects focused partial melt in the crust (e.g., Wittlinger et al., 1998) that has a similar density to the material to the south.

4. Discussion

4.1. Origin of anomalous upper mantle

The two most compelling and novel features of our model are in the upper mantle: the nearly continuous ring of low-density but variable-velocity mantle along the western and southern margins of Tarim (the western Tien Shan, Pamir, Kunlun Shan, and Altyn Tagh Fault) and the linear trend of low density focused beneath the Bachu uplift in southern (southwestern) Tarim.

Although melt-depletion driven by the Permian plume would leave behind a buoyant residue along the craton margins, this material would be stronger rather than weaker than its surroundings, at odds with the Cenozoic focusing of deformation along the margins of the Tarim block. More condemningly, Permian basalts occur over a region more than 1000 km long that cuts across the Tarim block rather than being focused along its edges. Therefore, we favor the interpretation that the lithospheric suture zones between Tarim and adjacent terranes serve as efficient conduits for mantle-derived fluids such as subduction-related volatiles (as also posited by Luo et al., 2001). Since hydration decreases viscosity (Guillot et al., 2001), this material would be weaker than its surroundings and experience proportionally higher strain rates under Cenozoic compression. Another possibility is the localized high temperature due to high shear stress (Wittlinger et al., 1998), which cannot be detected from the used tomography model, but is highlighted in our refinements.

The NW-SE strip of buoyant upper mantle beneath south Tarim underlies the Permian basalts and specifically the Bachu Uplift. Because this magma was created by the melting of thick, refractory mantle lithosphere by a mantle plume (Zhang et al., 2013; Xu et al., 2014), we hypothesize that the linear trend of low-density mantle is the result of plume-lithosphere interaction and reflects melt-depletion: decrease in garnet and clinopyroxene, and increase in #Mg. Such a residue would then have lower density but higher viscosity than the rest of Tarim and thus be more resistant to modern compression (e.g., Neil and Houseman, 1997).

This hypothesis unifies kinematic block models and continuum deformation models. As in the former, lithospheric-scale fault zones—Paleozoic continental sutures—do absorb most deformation, shunting strain away from Tarim. Nevertheless, this partitioning is not merely due to the pre-existence of faults; thermochemical processes (we hypothesize hydration) during or subsequent to accretion have weakened these suture zones. In addition, cratonization of south Tarim by Permian melt-depletion lends additional strength and allows far-field compressional stress to be transferred northward. Consistent with geodynamic modeling, lithospheric-scale variations play an important role in the localization of faults in this region (Cook and Royden, 2008), and the apparent discretization of central Asia into individual microplates is a predictable consequence of lithospheric-scale variations in rheology and density rather than the result of inherited fault geometry alone.

4.2. A trapped oceanic plateau?

The original nature of the lithosphere beneath Tarim before it was melt-depleted during the Permian is in question, as discussed above. Archean mafic gneisses and TTG suites (tonalite, trondhjemite, granodiorite as well as granites) are exposed at the surface in NE and SW Tarim (Long et al., 2011), whereas a drill core intercepted dioritic gneisses (Guo et al., 2005). Based on the nature of the exposed rocks on the margin of the craton, most workers assume the whole block has similar attributes and is a "typical" Archean craton, but others such as Neil and Houseman (1997) and Kusky and Mooney (2015) have suggested that it may be floored by oceanic plateau-type lithosphere at depth. Combining v_p, v_s, and geochronological information, Kusky and Mooney (2015) proposed that the Ordos basin is floored by a trapped oceanic plateau. Deep seismic sounding profiles have been conducted across the Tarim (Kunlun–Tarim profile, Li et al., 2001) and Ordos basins (Mandula–Yanchuan profile, Teng et al., 2010). The P-wave velocities of the two sections are similar, about 6.2 km/s in the upper crust and 6.6 km/s in the lower crust, and there is a high-velocity zone at the base of lower crust. By contrast, both blocks have high reported Pn velocity (McNamara et al., 1997; Xu et al., 2007). S-velocities (Bao et al., 2015) in these two basins show relatively slow upper crustal portions corresponding to the thick sedimentary basins but very fast velocities corresponding to cold rigid lithosphere extending deeper than 150 km. There are few earthquakes inside the Tarim and Ordos basins (Teng et al., 2014), and the two basins have very low heat flow (Kusky and Mooney, 2015) and $>$40 km crustal thickness (Teng et al., 2014). These geophysical features not only support the hypothesis that the crystalline basement and upper mantle beneath these two cratons are dominantly intermediate to mafic in composition but also suggest a similar origin for these two cratons.

The high-density lower crust and high v_p/v_s of the Tarim basement is similar to oceanic crust and lithosphere, and the crust (with sedimentary section removed) is about 30 km thick, which is similar to other oceanic plateaus such as Ontong–Java (see review by Kusky and Mooney, 2015). Additionally, the high-velocity mantle (thick sub-crustal mantle lithosphere, $>$100 km) is typical of oceanic plateaus (e.g., Mann and Taira, 2004; Kerr, 2014). Xenoliths in younger plutons show that the deep and old Archean rocks of the Tarim basin include gabbros that were derived from a metasomatized and depleted mantle reservoir (Zhang et al., 2012), then cut by potassic granites at 2.6–2.53 Ga, and metamorphosed at 1.85–1.80 Ga and 1.1–0.95 Ga (Zhang et al., 2012), events which would have significantly hydrated the oldest basement. Additionally, the Permian basalts sampled a hydrous but refractory lithosphere (Wei et al., 2015). Thus, the Tarim block seems to have grown by a series of melt-depletion events from an originally mafic–ultramafic thick lithosphere, showing that progressive differentiation of oceanic plateaus may be one way to form cratons (e.g., Kusky and Mooney, 2015). In general, it is thought that oceanic plateaus should have a refractory but anhydrous source, whereas continental flood basalts are derived from a hydrous but refractory source (e.g., Ernst, 2014). Although this may be true for extant oceanic plateaus that have not yet accreted and experienced subsequent melt-depletion and hydration events, the difference becomes blurred if cratons can form by multiple mechanisms, such as arc accretion and underplating of oceanic slabs (Kusky, 1993) or accretion of oceanic plateaus (e.g., Kusky and Kidd, 1992). The geo-

physical evidence discussed above shows that the northern margin of Tarim is variably underthrusting beneath Tien Shan.

5. Conclusions

In order to understand the origin of the Tarim block's stability amidst widespread Cenozoic deformation, we have developed a 3-D image of lithospheric density in central Asia from seismic velocity, gravity, topography, and crustal thermal models. At the broadest scale, Tarim contrasts with the rest of the region in that it is underlain by a thick, cold, and mafic lithospheric root, the origin of which is most plausibly an oceanic plateau. Yet there are finer-scale variations in velocity and/or density from which rheologic/lithologic anomalies can be inferred, and these localized strong/weak zones also influence the style and spatial extent of deformation.

A nearly continuous band of low-density mantle lithosphere underlies the actively deforming western and southern margins of Tarim, including the western Tien Shan, Pamir, Kunlun Shan, and Altyn Tagh fault. We suggest that this buoyant material is the result of hydration by mantle-derived fluids that have preferentially migrated along these Paleozoic continental suture zones. Thus, we suggest that these zones are not simply more susceptible to deformation than their surroundings because of the existence of faults but rather that thermochemical alterations from prior tectonism have reduced lithospheric viscosity.

In contrast to these weak zones, high-velocity but low-density upper mantle beneath the non-deforming southern (southwestern) Tarim underlies a region of Permian, plume-related basalts, from which we infer that the southern (southwestern) Tarim mantle lithosphere was further dehydrated and melt-depleted and thus its viscosity increased further. This strong region is capable of transmitting stress from the ongoing Indo-Eurasian collision northward to where we image the less depleted, thermally dense North Tarim lithosphere subducting beneath the Tien Shan. As such, we argue that the apparent discretization of central Asia into separate microplates is the result of strain partitioning by lithospheric-scale rheologic variations rather than the pre-existence or frictional properties of faults in the brittle crust.

Acknowledgements

We are very grateful to Dr. Xuewei Bao and Jiangtao Li for providing us their seismic velocity model. We appreciate Prof. Yigang Xu and Dr. Qiang Ma for valuable discussions. This research was funded by the Strategic Priority Research Program (B) of the Chinese Academy of Sciences (grant XDB18020201), National Natural Science Foundation of China (41504069) and State Key Laboratory of Isotope Geochemistry (SKBIG-RC-14-03) to YFD, the USGS Mendenhall postdoctoral fellowship to WL. Gravity, topography, and density modeling codes are available at https://github.com/wlevandowski-usgs/Tarim. Constructive comments from two anonymous reviewers have greatly improved the manuscript.

Appendix A. Supplementary material

Supplementary material related to this article can be found online at http://dx.doi.org/10.1016/j.epsl.2016.10.051.

References

Bao, X., Song, X., Li, J., 2015. High-resolution lithospheric structure beneath Mainland China from ambient noise and earthquake surface-wave tomography. Earth Planet. Sci. Lett. 417, 132–141.

Bendick, R., Bilham, R., Freymueller, J., Larson, K., Yin, G., 2000. Geodetic evidence for a low slip rate in the Altyn Tagh fault system. Nature 404, 69–72.

Brocher, T.M., 2005. Empirical relations between elastic wavespeeds and density in the Earth's crust. Bull. Seismol. Soc. Am. 95, 2081–2092.

Calignano, E., Sokoutis, D., Willingshofer, E., Gueydan, F., Cloetingh, S., 2015. Strain localization at the margins of strong lithospheric domains: insights from analog models. Tectonics 34, 396–412.

Christensen, N.I., 2004. Serpentinites, peridotites, and seismology. Int. Geol. Rev. 46, 795–816.

Christensen, N.I., Mooney, W.D., 1995. Seismic velocity structure and composition of the continental crust: a global view. J. Geophys. Res. 100, 9761–9788.

Cook, K.L., Royden, L.H., 2008. The role of crustal strength variations in shaping orogenic plateaus, with application to Tibet. J. Geophys. Res. 113. http://dx.doi.org/10.1029/2007JB005457.

Cowgill, E., Gold, R.D., Xuanhua, C., Xiao-Feng, W., Arrowsmith, J.R., Southon, J., 2009. Low Quaternary slip rate reconciles geodetic and geologic rates along the Altyn Tagh fault, northwestern Tibet. Geology 37, 647–650.

Deng, Y., Zhang, Z., Badal, J., Fan, W., 2014. 3-D density structure under South China constrained by seismic velocity and gravity data. Tectonophysics 627, 159–170.

England, P., McKenzie, D., 1982. A thin viscous sheet model for continental deformation. Geophys. J. Int. 70, 295–321.

Ernst, 2014. Large Igneous Provinces. Cambridge University Press. 653 pp.

Feng, C.G., Liu, S.W., Wang, L.S., Li, C., 2009. Present-Day Geothermal Regime in Tarim Basin, Northwest China. Chin. J. Geophys. 52, 1237–1250.

Godey, S., Deschamps, F., Trampert, J., Snieder, R., 2004. Thermal and compositional anomalies beneath the North American continent. J. Geophys. Res. 109.

Guillot, S., Hattori, K.H., de Sigoyer, J., Nägler, T., Auzende, A.-L., 2001. Evidence of hydration of the mantle wedge and its role in the exhumation of eclogites. Earth Planet. Sci. Lett. 193 (1), 115–127.

Guo, Z.-J., Yin, A., Robinson, A., Jia, C.-Z., 2005. Geochronology and geochemistry of deep-drill-core samples from the basement of the central Tarim basin. J. Asian Earth Sci. 25, 45–56.

Hacker, B.R., Abers, G.A., 2004. Subduction Factory 3: an Excel worksheet and macro for calculating the densities, seismic wave speeds, and H_2O contents of minerals and rocks at pressure and temperature. Geochem. Geophys. Geosyst. 5.

Hammond, W.C., Humphreys, E.D., 2000. Upper mantle seismic wave velocity-effects of realistic partial melt geometries. J. Geophys. Res. 105, 10975–10986.

Hendrix, M.S., Dumitru, T.A., Graham, S.A., 1994. Late Oligocene–early Miocene unroofing in the Chinese Tian Shan: an early effect of the India–Asia collision. Geology 22, 487–490.

Hsü, K.J., 1988. Relict back-arc basins: principles of recognition and possible new examples from China. In: New Perspectives in Basin Analysis. Springer, pp. 245–263.

Humphreys, E.D., Dueker, K.G., 1994. Physical state of the western US upper mantle. J. Geophys. Res. 99, 9635–9650.

Kao, H., Gao, R., Rau, R.-J., Shi, D., Chen, R.-Y., Guan, Y., Wu, F.T., 2001. Seismic image of the Tarim basin and its collision with Tibet. Geology 29 (7), 575–578.

Kerr, A.C., 2014. Oceanic plateaus. In: Rudnick, R. (Ed.), The Crust, Treatise on Geochemistry, 2nd ed. Elsevier, Amsterdam.

Kusky, T.M., 1993. Collapse of Archean orogens and the origin of late- to post-kinematic granitoids. Geology 21, 925–929.

Kusky, T.M., Kidd, W.S.F., 1992. Remnants of an Archean oceanic plateau, Belingwe greenstone belt, Zimbabwe. Geology 20 (1), 43–46.

Kusky, T., Mooney, W., 2015. Is the Ordos basin floored by a trapped oceanic plateau? Earth Planet. Sci. Lett. 429, 197–204.

Lachenbruch, A.H., Morgan, P., 1990. Continental extension, magmatism and elevation; formal relations and rules of thumb. Tectonophysics 174, 39–62.

Lee, C.-T., Yin, Q., Rudnick, R.L., Jacobsen, S.B., 2001. Preservation of ancient and fertile lithospheric mantle beneath the southwestern United States. Nature 411, 69–73.

Lei, J., Zhao, D., 2007. Teleseismic P-wave tomography and the upper mantle structure of the central Tien Shan orogenic belt. Phys. Earth Planet. Inter. 162, 165–185.

Levandowski, W., Jones, C.H., Shen, W., Ritzwoller, M.H., Schulte-Pelkum, V., 2014. Origins of topography in the western US: mapping crustal and upper mantle density variations using a uniform seismic velocity model. J. Geophys. Res. 119, 2375–2396.

Levandowski, W., Boyd, O.S., Briggs, R.W., Gold, R.D., 2015. A random-walk algorithm for modeling lithospheric density and the role of body forces in the evolution of the Midcontinent Rift. Geochem. Geophys. Geosyst. 16. http://dx.doi.org/10.1002/2015GC005961.

Li, Q., Gao, R., Lu, D., Li, J., Fan, J., Zhang, Z., Liu, W., Li, Y., Yan, Q., Li, D., 2001. An explosive seismic sounding profile across the transition zone between west Kunlun Mts. and Tarim Basin. Sci. China Earth Sci. 44, 666–672.

Li, Z., Steve, R., Li, Z., Wei, B., Wang, H., Gennady, S., Vitaly, B., 2009. Tomographic image of the crust and upper mantle beneath the western Tien Shan from the MANAS broadband deployment: possible evidence for lithospheric delamination. Tectonophysics 477, 49–57.

Liu, H., Somerville, I.D., Lin, C., Zuo, S., 2016. Distribution of Palaeozoic tectonic superimposed unconformities in the Tarim Basin, NW China: significance for the evolution of palaeogeomorphology and sedimentary response. Geol. J. 51 (4), 627–651. http://dx.doi.org/10.1002/gj.2664.

Long, X., Yuan, C., Sun, M., Kröner, A., Zhao, G., Wilde, S., Hu, A., 2011. Reworking of the Tarim Craton by underplating of mantle plume-derived magmas: evidence from Neoproterozoic granitoids in the Kuluketage area, NW China. Precambrian Res. 187, 1–14.

Luo, Z., Xiao, X., Cao, Y., Mo, X., Su, S., Deng, J., Zhang, W., 2001. The Cenozoic mantle magmatism and motion of lithosphere on the north margin of the Tibetan Plateau. Sci. China Earth Sci. 44, 10–17.

Maceira, M., Ammon, C.J., 2009. Joint inversion of surface wave velocity and gravity observations and its application to central Asian basins shear velocity structure. J. Geophys. Res. 114, B02314.

Mann, P., Taira, A., 2004. Global tectonic significance of the Solomon Islands and Ontong Java Plateau convergent zone. Tectonophysics 389, 137–190.

McNamara, D., Walter, W., Owens, T., Ammon, C., 1997. Upper mantle velocity structure beneath the Tibetan Plateau from Pn travel time tomography. J. Geophys. Res. 102, 493–505.

Mooney, W.D., Kaban, M.K., 2010. The North American upper mantle: density, composition, and evolution. J. Geophys. Res. 115, B12424.

Neil, E.A., Houseman, G.A., 1997. Geodynamics of the Tarim Basin and the Tian Shan in central Asia. Tectonics 16, 571–584.

Pavlis, N.K., Holmes, S.A., Kenyon, S.C., Factor, J.K., 2012. The development and evaluation of the Earth Gravitational Model 2008 (EGM2008). J. Geophys. Res. 117, B04406.

Pérez-Gussinyé, M., Lowry, A.R., Watts, A.B., Velicogna, I., 2004. On the recovery of effective elastic thickness using spectral methods: examples from synthetic data and from the Fennoscandian Shield. J. Geophys. Res. 109, B10409. http://dx.doi.org/10.1029/2003JB002788.

Sato, H., Sacks, I.S., Murase, T., 1989. The use of laboratory velocity data for estimating temperature and partial melt fraction in the low-velocity zone: comparison with heat flow and electrical conductivity studies. J. Geophys. Res. 94 (B5), 5689–5704.

Schutt, D.L., Lesher, C.E., 2010. Compositional trends among Kaapvaal Craton garnet peridotite xenoliths and their effects on seismic velocity and density. Earth Planet. Sci. Lett. 300, 367–373.

Sengör, A., 1979. Mid-Mesozoic closure of Permo-Triassic Tethys and its implications. Nature 279, 590–593.

Sheehan, A.F., Solomon, S.C., 1991. Joint inversion of shear wave travel time residuals and geoid and depth anomalies for long-wavelength variations in upper mantle temperature and composition along the Mid-Atlantic Ridge. J. Geophys. Res. 96 (B12), 19981–20009.

Sun, Y., Dong, S., Zhang, H., Li, H., Shi, Y., 2013. 3D thermal structure of the continental lithosphere beneath China and adjacent regions. J. Asian Earth Sci. 62, 697–704.

Tapponnier, P., Molnar, P., 1976. Slip-line field theory and large-scale continental tectonics. Nature 264 (5584), 319–324.

Tapponnier, P., Zhiqin, X., Roger, F., Meyer, B., Arnaud, N., Wittlinger, G., Jingsui, Y., 2001. Oblique stepwise rise and growth of the Tibet Plateau. Science 294, 1671–1677.

Teng, J., Deng, Y., Badal, J., Zhang, Y., 2014. Moho depth, seismicity and seismogenic structure in China mainland. Tectonophysics 627, 108–121.

Teng, J., Wang, F., Zhao, W., Zhang, Y., Zhang, X., Yan, Y., Zhao, J., Li, M., Yang, H., Zhang, H., 2010. Velocity structure of layered block and deep dynamic process in the lithosphere beneath the Yinshan orogenic belt and Ordos Basin. Chin. J. Geophys. 53, 67–85.

Vinnik, L., Aleshin, I., Kaban, M., Kiselev, S., Kosarev, G., Oreshin, S., Reigber, C., 2006. Crust and mantle of the Tien Shan from data of the receiver function tomography. Izv. Phys. Solid Earth 42, 639–651.

Watts, A.B., 2001. Isostasy and Flexure of the Lithosphere. Cambridge University Press.

Wei, X., Xu, Y.-G., Luo, Z.-Y., Zhao, J.-X., Feng, Y.-X., 2015. Composition of the Tarim Mantle plume: constraints from clinopyroxene antecrysts in the early Permian Xiaohaizi dykes, NW China. Lithos 230, 69–81.

Windley, B., Allen, M., Zhang, C., Zhao, Z., Wang, G., 1990. Paleozoic accretion and Cenozoic redeformation of the Chinese Tien Shan range, central Asia. Geology 18, 128–131.

Wittlinger, G., Tapponnier, P., Poupinet, G., Mei, J., Danian, S., Herquel, G., Masson, F., 1998. Tomographic evidence for localized lithospheric shear along the Altyn Tagh fault. Science 282, 74–76.

Xie, J., Ritzwoller, M.H., Shen, W., Yang, Y., Zheng, Y., Zhou, L., 2013. Crustal radial anisotropy across eastern Tibet and the western Yangtze craton. J. Geophys. Res. 118, 4226–4252.

Xu, Y., Li, Z., Roecker, S.W., 2007. Uppermost mantle structure and its relation with seismic activity in the central Tien Shan. Geophys. Res. Lett. 34. http://dx.doi.org/10.1029/2007GL029708.

Xu, Y.-G., Wei, X., Luo, Z.-Y., Liu, H.-Q., Cao, J., 2014. The Early Permian Tarim Large Igneous Province: main characteristics and a plume incubation model. Lithos 204, 20–35.

Yang, Y., Liu, M., 2002. Cenozoic deformation of the Tarim plate and the implications for mountain building in the Tibetan Plateau and the Tian Shan. Tectonics 21, 9-1–9-17.

Yin, A., Rumelhart, P., Butler, R., Cowgill, E., Harrison, T., Foster, D., Ingersoll, R., Qing, Z., Xian-Qiang, Z., Xiao-Feng, W., 2002. Tectonic history of the Altyn Tagh fault system in northern Tibet inferred from Cenozoic sedimentation. Geol. Soc. Am. Bull. 114, 1257–1295.

Zhang, C.L., Li, Huaikun, Santosh, M., Li, Zhengxiang, Zou, Haibo, Wang, Hongyan, Ye, Haimin, 2012. Precambrian evolution and cratonization of the Tarim Block, NW China: petrology, geochemistry, Nd-isotopes and U–Pb zircon geochronology from Archaean gabbro-TTG–potassic granite suite and Paleoproterozoic metamorphic belt. J. Asian Earth Sci. 47, 5–20.

Zhang, C.-L., Zou, H.-B., Li, H.-K., Wang, H.-Y., 2013. Tectonic framework and evolution of the Tarim Block in NW China. Gondwana Res. 23, 1306–1315.